

Electronic Theses and Dissertations, 2004-2019

2012

Laser Spark Ignition of Counter-flow Diffusion Flames: Effects of diluents and diffusive-thermal properties

Fidelio Sime Segura
University of Central Florida

 Part of the [Mechanical Engineering Commons](#)
Find similar works at: <https://stars.library.ucf.edu/etd>
University of Central Florida Libraries <http://library.ucf.edu>

This Masters Thesis (Open Access) is brought to you for free and open access by STARS. It has been accepted for inclusion in Electronic Theses and Dissertations, 2004-2019 by an authorized administrator of STARS. For more information, please contact STARS@ucf.edu.

STARS Citation

Segura, Fidelio Sime, "Laser Spark Ignition of Counter-flow Diffusion Flames: Effects of diluents and diffusive-thermal properties" (2012). *Electronic Theses and Dissertations, 2004-2019*. 4681.
<https://stars.library.ucf.edu/etd/4681>

LASER SPARK IGNITION OF COUNTER-FLOW DIFFUSION FLAMES: EFFECTS OF DILUENTS AND DIFFUSIVE-
THERMAL PROPERTIES

by

FIDELIO SIME SEGURA
B.E. Stevens Institute of Technology, 2010

A thesis submitted in partial fulfillment of the requirements
for the degree of Masters in Science in Mechanical Engineering
in the department of Mechanical, Materials and Aerospace Engineering
in the College of Engineering and Computer Science
at the University of Central Florida
Orlando, Florida

Spring Term
2012

Major Professors: Weiwei Deng and Ruey-Hung Chen

©2012 Fidelio Sime Segura

ABSTRACT

A pulsed Nd:YAG laser is used to study laser spark ignition of methane counter-flow diffusion flames with the use of helium and argon as diluents to achieve a wide range of variations in transport properties. The global strain rate and Damköhler number on successful ignition were investigated for the effects of Lewis number and transport properties, which are dependent on the diluent type and dilution level. A high-speed camera is used to record the ignition events and a software is used for pre-ignition flow field and mixing calculations. It is found that the role of effective Lewis number on the critical global strain rate, beyond which ignition is not possible, is qualitatively similar that on the extinction strain rate. With the same level of dilution, the inert diluent with smaller Lewis number yields larger critical global strain rate. The critical Damköhler number below which no ignition is possible is found to be within approximately 20% for all the fuel-inert gas mixtures studied. When successful ignition takes place, the ignition time increases as the level of dilution of argon is increased. The ignition time decreases with increasing level of helium dilution due to decreases in thermal diffusion time, which causes rapid cooling of the flammable layer during the ignition process. However, the critical strain for ignition with helium dilution rapidly decreases as the dilution level is increased. The experimental results show that with the increase of strain rate the time to steady flame decreases, and that with the increase of dilution level time for the flame to become steady increases. For the same level of dilution, the time for steady flame is observed to be longer for He-diluted flames than for Ar-diluted flames due to its thermal diffusivity being larger than that of Ar.

Dedicated to my mother, Elvira, for the unconditional support she has always given me while I pursue my dreams.

ACKNOWLEDGMENTS

It would have not been possible to write this masters thesis without the help and support of the people around me, to only some of whom it is possible to give particular mention here.

I would like to acknowledge the advice and guidance of Dr. Weiwei Deng and Dr. Ruey-hung Chen, committee co-chairs. It was their patience, help, good advice and support that allowed the completion of this work. I would also like to acknowledge Mrs. Yan Wei for her theoretical contributions and numerical results contained in this thesis, without which this study would have not been successful. I also thank the DENG lab members for their help with experimental setup as well as for the questions regarding this work.

I acknowledge the Florida Center for Advanced Aero-Propulsion (FCAAP) for their financial support for this project.

I would like to thank my family, especially my parents and my sisters for their unconditional support and always making sure I was alright. I would also like to thank my cousin Winston Martinez as well as my friends Edward Carrasco and Edwin Rodriguez for always listening to me when I needed it the most.

TABLE OF CONTENTS

LIST OF FIGURES.....	vii
LIST OF TABLES.....	viii
CHAPTER 1: INTRODUCTION.....	1
1.1 Motivation.....	1
1.2 Objectives.....	2
CHAPTER 2: LITERATURE REVIEW	4
CHAPTER 3: EXPERIMENTAL AND NUMERICAL METHODOLOGIES.....	7
3.1 Experiment apparatus.....	7
3.3 Experimental and Numerical Procedures	12
CHAPTER 4: ANALYSIS	21
4.1 Ignition position	21
4.2 Visual observations	22
4.3 Critical strain rate, Kg,ig	24
4.4 Critical Damköhler number for ignition	28
4.5 Time to flame kernel/induction time, tk	31
4.6 Time to steady flame	34
CHAPTER 5: CONCLUSION.....	36
5.1 Summary	36
5.2 Future work.....	38
PUBLICATION LIST	39
REFERENCES.....	40

LIST OF FIGURES

Figure 1 – Experimental setup	7
Figure 2 – (a) Inner nozzle (b) Counterflow burner assembled	8
Figure 3 – (a) Counter-flow burner (b) Counter-flow diffusion flame	9
Figure 4 - Phantom v12.1 camera	12
Figure 5 - (a) Calculation domain (b) Grid distribution	16
Figure 6 - Laser spark image using microscope lens	18
Figure 7 - Ignition position vs. global strain rate	21
Figure 8 - First successful ignition of counter-flow flame in this work	22
Figure 9 - Ignition process (t = 0 at spark deposition) – (a) Identification of time to flame kernel formation (Processed with ImageJ to enhance visibility); (b) & (c) flame development process; (d) time to steady flame.....	23
Figure 10 - Time to flame kernel (tk ; open symbols) and characteristic thermal diffusion time (τd ; closed symbols) vs. global strain rate	25
Figure 11 - S-curve for diffusion flames	27
Figure 12 - Flammable layer thickness vs. global strain rate	29
Figure 13 - Thermal diffusion time scale vs. convective flow time scale.....	31
Figure 14 - Non-dimensional ignition to diffusion time vs. global flow time	33
Figure 15 - Time to steady flame vs. global strain rate.....	35
Figure 16 - Richardson number vs. global strain rate	35

LIST OF TABLES

Table 1 – Quantel Brilliant laser parameters ($\lambda = 1064 \text{ nm}$)	10
Table 2 – Phantom v12.1 pixels to maximum frames per second	19
Table 3 - Properties related to flame extinction and ignition of CH ₄ and diluted CH ₄	20
Table 4 - Effective and fuel Lewis number for various dilution levels	25

CHAPTER 1: INTRODUCTION

1.1 Motivation

A premixed flame is a flame in which the fuel and oxidizer have been homogeneously mixed before it reaches the flame front. Non-premixed flames, also known as diffusion flames, are those flames in which fuel and oxidizer are mixed as they approach the ignition source. The distinction between the two flames is that in diffusion flames the burning rate is determined by the rate at which the fuel and oxidizer come together and for premixed flames it is predominantly dominated by chemistry. Premixed flame ignition and extinction phenomena have been well studied by the combustion community in the past [1-4], but great deals of unknowns remain for ignition of diffusion flames. Ignition is defined as the start of chemical reaction between fuel and oxidizer, while extinction is when this reaction is stopped.

Nowadays more than 80% of the energy production is based on combustion, and with a strong and ever increasing demand for energy a lot of focus is being given to improve efficiency and reduce waste of resources [5]. The types of flames used in industrial combustion are very complex, typically in the turbulent regime as well as an array of other irregularities that make it very difficult to perform experimental studies even with current advances in technology. In order to deal with these obstacles scientists have developed various methods over the years to simplify these problems and try to gain a better understanding of combustion in diffusion flames. One of the most used methods, and the one on which this study is based, is to take a complex turbulent flame as an ensemble of small scale laminar flames. This technique is known under the name of "flamelet model", which was first introduced by Williams [6].

1.2 Objectives

The counter-flow configuration for diffusion flames consist of two opposed jets of fuel and oxidizer and shares some common one-dimensional features with laminar flamelets and have been used to gain insight into combustion characteristics of laminar and turbulent non-premixed flames [7]. Forced ignition is a process in which a mechanism or system is used to start the chemical reaction between fuel and oxidizer. Relatively few studies have been performed on the forced ignition processes of laminar non-premixed combustion [8-10]. These studies will be further discussed in Chapter 2 of this thesis. In these studies the effects of diluents type as well as diffusive and thermal transport properties are largely left unaddressed. Furthermore, the ignition delay time has not been reported in the non-premixed counter-flow system. These unresolved issues are the focus of this study.

Laser spark is used as the ignition source due to it being the least intrusive method of forced ignition and it is adopted in laminar methane-air counter-flow diffusion flames to further understanding of the ignition behavior for a wide range of strain rates and diffusive-thermal properties. Helium and argon gases are the diluents for such purposes because both are very similar (same heat capacity) and largely differ in thermal diffusive properties, which is the focus of this study. The ignition process of combustion gases produced by a laser spark is described in detail in [11]. When a laser beam of irradiance in the order of 10^{10} W/cm^2 interacts with combustion gases, a plasma of high temperature ($\sim 10^6 \text{ K}$) and high pressure ($\sim 10^3 \text{ atm}$) is created at the end of the laser pulse. This extreme condition relative to the ambient conditions of the gases leads to the development of a rapidly expanding shock wave that is strong enough to ignite combustible media [11]. Lasers also allow for change in spark

position with the use of stages and optical devices to ensure optimal ignition condition as well as spark parameters (energy, size) that are very repeatable with small errors [12].

CHAPTER 2: LITERATURE REVIEW

Topics of particular importance in counter-flow flames include extinction processes and they have been experimentally and numerically studied [13-19]. Many studies have been done on the effect of transport properties (preferential diffusion, effective Lewis number, and Schmidt number) on extinction of counter-flow flames [17, 18, 20, 21] and flame lift-off phenomena [22]. The effect of Lewis number (ratio of thermal diffusivity to mass diffusivity) on diffusion flame extinction has been investigated by using diluent gases of helium and argon that have the same molar specific heats to reveal the effects of Lewis number (i.e. diffusive-thermal effects) independent of the effect of heat capacity. Chen et al. [20] and Park et al. [21] analyzed the effects of diluents on the extinction of diffusion flames in terms of effective Lewis number, which is the weighted value of the fuel and oxidizer Lewis numbers [23]. Le_e , is defined as [23]:

$$Le_e \equiv \frac{L_F + A_F L_O}{1 + A_F} \quad (1)$$

where L_F and L_O are fuel and oxidizer Lewis number, respectively, and A_F is the “equivalence ratio” or “mixture strength” or the premixed burning regime of the premixed regime of the diffusion flame. The equivalence ratio is defined as $A_F \equiv \nu Y_F / Y_O$ where $\nu = 3.99$ for $CH_4 - O_2$ is the stoichiometric oxidizer-to-fuel mass ratio (= 3.99 for $CH_4 - O_2$) and Y_F and Y_O are the mass fractions of fuel and oxidizer in their respective stream.

The effective Lewis number (Le_e) successfully explained extinction phenomena for fuels diluted with inert gases that possess vastly different diffusivities (such as Argon and Helium) [20]. It was concluded over a wide range of combinations of diluent type and dilution level, the combinations producing $Le_e < 1$ leads to larger extinction strain rates. However, it is not known whether it can help explain the ignition phenomena, such as the maximum strain rate for successful ignition and the ignition

delay time. Prior to successful ignition thermal and concentration gradients do not exist for diffusive-thermal effects to manifest themselves which means that effective Lewis number might not be able to predict phenomena taking place during ignition.

The flamelet model consists of taking a complex turbulent flame as an ensemble of small scale laminar flames [6]. For the opposed jet configuration (i.e. counter-flow) the critical Reynolds number for turbulent flow is in the range of 10^4 based on the inner nozzle diameter (d_i) and it is calculated as $Re = U \frac{d_i}{\nu}$ [24, 25]. U is the mass averaged velocity and ν is the kinematic viscosity. In this work Reynolds number ranges from the low hundreds to the high hundreds, well below the critical Reynolds number and in the laminar regime. For example for the pure methane at a strain rate of 420 s^{-1} Reynolds number was calculated to be 796.

As mentioned in Chapter 1 section 2, few studies on ignition of counter-flow diffusion flames have been conducted. Phuoc [8] studied the minimum ignition energy associated with laser spark ignition and concluded that the ignition energy obtained by the laser spark ignition does not differ greatly from that obtained by the electric spark ignition. Phuoc and Chen [9] also studied the effect of nitrogen dilution on the ignition stability with the use of laser-induced spark. Other numerical and theoretical studies on ignition of counterflow diffusion flames have been performed to mainly reveal effects of spark position, spark duration, spark energy, strain rate, ignition probability, and minimum ignition energy level [10].

Phuoc [11] provided a review of the fundamentals and applications of laser spark ignition, in which all phenomena regarding the ignition process in premixed flames are discussed. From this review and results obtained in this study, laser-induced gas breakdown was researched. The absorption of such

laser spark energy for wavelengths greater than 300 nm by gases such as air and argon is reported to be between 8% and 12% [26]. Another important step was to gain background on how to optimize the ignition process as well as what to expect once ignition was successful. In momentum matched counter-flow flames the position of the mixing layer region (i.e. ignitable region) lies near the mid-plane of the two burners, allowing easy access by the laser spark [11, 20]. Due to the small mixture fraction of pure and diluted CH₄-air flames, the stoichiometric plane is always on the air side of the mixing layer [18].

This thesis is structured as follows: in the next chapter the experimental setup and techniques used to study the ignition process will be presented, and then visual observations will be described for pure methane flames as well as with the addition of diluents. Then the definition of critical strain rate will be given, after which, Chapter 4 will address critical Damköler number for ignition and time to flame kernel. Next, a brief discussion on time to steady flame will follow. Finally, conclusions will be drawn from the results and discussions presented as well as future work needed.

CHAPTER 3: EXPERIMENTAL AND NUMERICAL METHODOLOGIES

3.1 Experiment apparatus

The experimental apparatus is sketched in Fig. 1. It consists of an axisymmetric counter-flow burner, an Nd:YAG laser, three-axis motion controllers (for precise location of spark down to the $1\ \mu\text{m}$), optical devices (i.e., a 10x beam expander and a 100-mm focal lens), and a high-speed camera. Each side of the burner was composed of inner main nozzles (for fuel/oxidizer) and outer nozzles (for N_2), with the latter being used to shield the ignition process from external disturbances. The diameters of the inner and outer nozzles are 8.9 mm and 13.56 mm, respectively. The inner nozzle can be seen in Fig. 2a and the sketch of the complete assembly observed in Fig. 2b below.

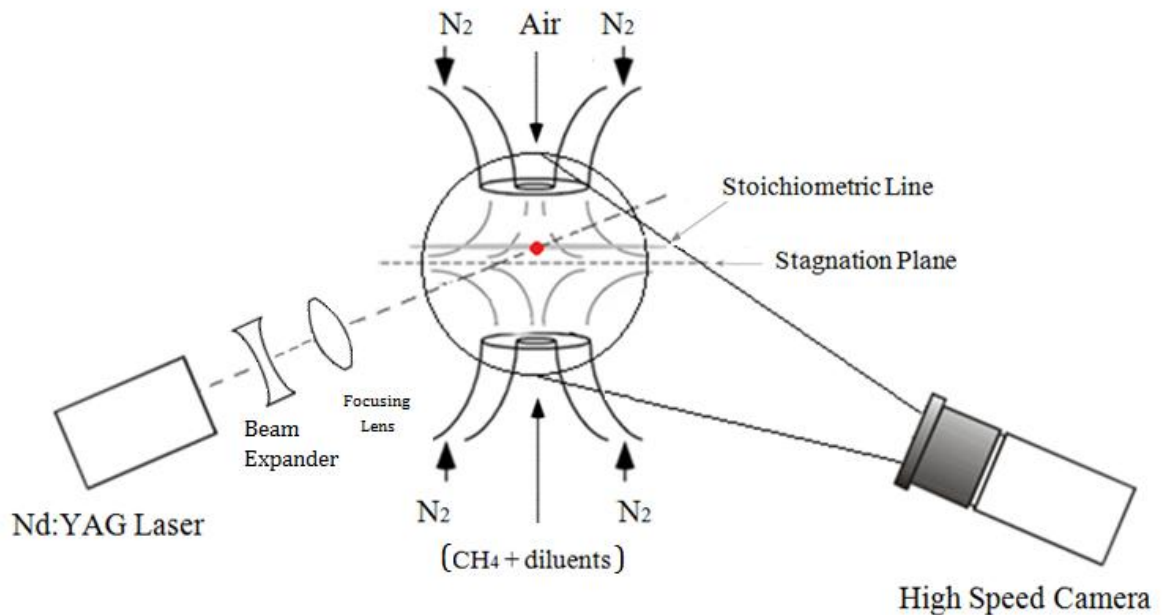
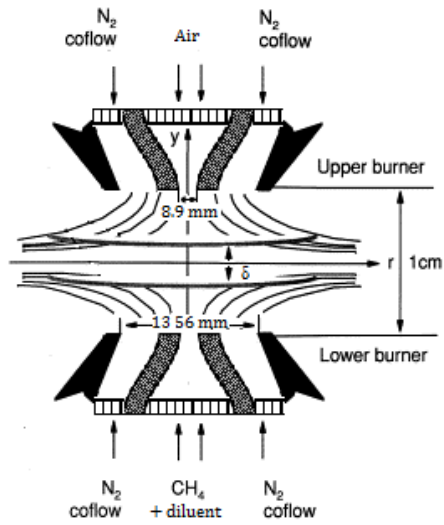


Figure 1 – Experimental setup



Figure 2 – (a) Inner nozzle



(b) Counterflow burner assembled

The burner and the laser were attached onto a three-axis and a two-axis motion control system for precise alignment of spark location. These axis were controlled using a simple G-code program (software used to operate CNC machinery) that provided steps in the μm scale. The burner consists of two nozzle sets (each with an inner and outer channel) with three gas inlets. In order to assure that they are concentric four rods are used to connect them (see Fig. 3a) and a level used to adjust the nuts for height at each point. The bottom nozzle assembly was attached to the L-bracket first keeping the surfaces parallel in order to keep the burner from being tilted. The top nozzle assembly was then added and adjusted to be concentric and parallel to the bottom nozzle.

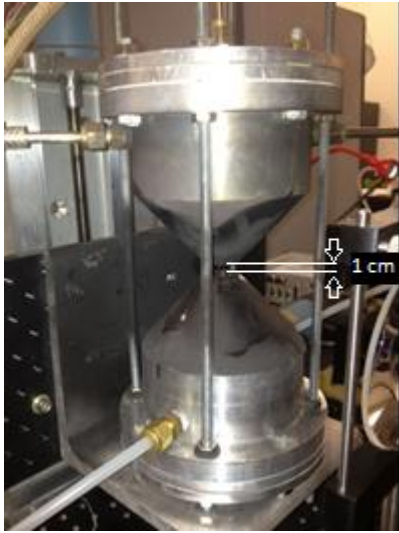


Figure 3 – (a) Counter-flow burner



(b) Counter-flow diffusion flame

The burner was adjusted to keep a separation distance between the two nozzles of 1 cm. In Fig. 3b a fully established and steady counter-flow diffusion flame using the burner in Fig. 3a can be observed, with pure methane being used as the fuel. As expected [Ref. 18], in Fig. 3b the flame lies closer to the air side. The high-speed camera was mounted on a hydraulic jack in order to adjust the height to match that of the burner separation. The laser was fixed in the vertical direction. The burner surfaces as well as the beam dump were coated with black high temperature resistant paint in order to avoid laser beam reflections. Laser sparks were generated by pulsing a Nd:YAG laser (Quantel Brilliant; 1064 nm with a pulse duration of 3.5 ns) which has an energy per pulse of 380 mJ. The laser pulse was expanded using a 10x beam expander with an inlet diameter of 2 mm, and then focused using a 100mm focal length lens. Table 1 shows the laser parameters provided by the manufacturer and calculated for this work.

Table 1 – Quantel Brilliant laser parameters ($\lambda = 1064 \text{ nm}$)

Repetition Rate (Hz)	10
Energy per Pulse (mJ)	380
Laser Power (MW)	102
Pulse Duration FWHM (ns)	3.5
Beam Diameter (mm)	≈ 6
Beam Expander Inlet Diameter (mm)	2
Beam Diameter after expander (mm)	20
Focal Length (mm)	100
Laser Spot Diameter (μm)	2.03
Irradiance ($\frac{W}{\text{cm}^2}$)	4.5×10^{17}

In order to place these optical devices in good alignment with the laser apparatus and the counter-flow burner a rail was necessary as well as posts and a mini stage with manual vertical adjustment for the beam expander. The focused spark region was calculated to have a diameter of $\sim 2 \mu\text{m}$ and a length of $\sim 1 \text{ mm}$ using a method described in [27] (Eqns.(2) and (3) given below); the length was confirmed using a microscope image taken with a high speed camera (described below) with a 10x magnifying lens. These dimensions of laser energy deposition spot are smaller than the thickness of the flammable layer in the counter-flow mixing region.

$$r = \left(\frac{2\lambda}{\pi}\right) \frac{f}{d} \quad (2)$$

$$l = (\sqrt{\pi} - 1) \frac{\theta}{d} f^2 \quad (3)$$

θ, r, l, f, d and λ denote beam divergence, radius and length in terms of spot size, focal length, beam diameter and laser wavelength respectively. In the first version of the experiment the laser was completely fixed. Also no focus lens was used. The spark produced by the laser at this stage met the irradiance threshold necessary for ignition [11] mentioned in the Objectives section of the first chapter of this work. A beam expander was deemed necessary due to the length of the spark being larger than the ignitable region of the flammable layer. The beam expander was only adjustable in the vertical direction, which meant some centering was needed in the horizontal direction. The laser was mounted onto a two-axis motion controller in order to easily align with the inlet of the beam expander. Inlet diameter of beam expander was measured to be 2 mm.

Figure 4 shows the Phantom v12.1 camera used to record the ignition phenomena in this experiment. This camera communicates with the computer via Ethernet connection. The manufacturer also provides very user friendly software to operate the camera. A TAMRON 60 mm F/2 Macro lens was used with the camera, with the lens always fully opened to allow for maximum light absorption. An extra Ethernet card had to be added to the computer, because the camera needs special settings in order to communicate with the computer as well as to keep internet connectivity for easy back-up of data obtained in experiments.



Figure 4 - Phantom v12.1 camera

Other needs in the experimental setup were addressed. Among these was the addition gas lines as diluents were added as well as the calibration and addition of mass flow controllers. The flow controllers used in the experiment were constantly checked for accuracy and adjusted accordingly. The beam dump was changed after the addition of the beam expander, according to calculations and distance from the focal point to the beam dump. Lastly the attachment of the burner onto the motion controller was adjusted in order to allow space for the larger beam dump.

3.3 Experimental and Numerical Procedures

This experiment relied heavily on using accurate location of the best area for successful ignition. Due to the size of the spark as well as the small ignitable region the help of software was needed. FLUENT V6.3 was used to calculate the flammable layer thickness and the precise location where the stoichiometric condition (i.e. the stoichiometric mass fraction which is defined below, Y_{St}) exists. For

consistency, the laser spark was always focused on the intersection of the plane and the axis of symmetry of the burners. The thickness of the flammable layer was then used to determine the characteristic heat diffusion time.

$$Y_{st} = \frac{Y_{CH_4}}{Y_{CH_4} + Y_{diluent} + 2(Y_{O_2} + 3.76Y_{N_2})} \quad (4)$$

In order to obtain the energy deposition positions prior to the experiments, the governing equations of mass, momentum, chemical species for a cold flow are solved using FLUENT code. The governing equations used in the code are given below.

Governing equations

1. The mass conservation equation

The equation for continuity equation is written as follows:

$$\frac{\partial \rho}{\partial t} + \nabla \cdot (\rho \vec{v}) = S_m \quad (5)$$

Equation 1 is the general form of the mass conservation equation and is valid for incompressible as well as compressible flows. The source S_m is the mass added to the continuous phase from the dispersed second phase (e.g., due to vaporization of liquid droplets) and any user-defined sources.

For 2D axisymmetric geometries used in the paper, the continuity equation can be written as

$$\frac{\partial \rho}{\partial t} + \frac{\partial}{\partial x}(\rho v_x) + \frac{\partial}{\partial r}(\rho v_r) + \frac{\rho v_r}{r} = S_m \quad (6)$$

Where x is the axial coordinate, r is the radial coordinate, v_x is the axial velocity, and v_r is the radial velocity.

2. Momentum conservation equation

Conservation of momentum is described by [28]

$$\frac{\partial}{\partial t}(\rho\vec{v}) + \nabla \cdot (\rho\vec{v}\vec{v}) = -\nabla p + \nabla \cdot (\overline{\overline{\tau}}) + \rho\vec{g} + \vec{F} \quad (7)$$

Where p is the static pressure, $\overline{\overline{\tau}}$ is the stress tensor, and $\rho\vec{g}$ and \vec{F} are the gravitational body force and external body forces (e.g., that arise from interaction with the dispersed phase), respectively.

The stress tensor $\overline{\overline{\tau}}$ is given by

$$\overline{\overline{\tau}} = \mu[(\nabla\vec{v} + \nabla\vec{v}^T) - \frac{2}{3}\nabla \cdot \vec{v}I] \quad (8)$$

where μ is the molecular viscosity, I is the unit tensor, and the second term on the right hand side is the effect of volume dilation.

3. Species transport equations

For the local mass fraction of the i th species, Y_i , the conservation equation takes the following general form:

$$\frac{\partial}{\partial t}(\rho Y_i) + \nabla \cdot (\rho\vec{v}Y_i) = -\nabla \cdot \vec{J}_i + R_i + S_i \quad (9)$$

Where R_i is the net rate of production of species i by chemical reaction and S_i is the rate of creation by addition from the dispersed phase plus any other sources. Since only cold flow is of interest here, R_i and S_i equal to 0. An equation of this form will be solved for $N-1$ species where N is the total number of fluid phase chemical species present in the system.

4. Mass diffusion in laminar flows

In Equation (10), \vec{J}_i is the diffusion flux of species I, which arises due to concentration gradients.

$$\vec{J}_i = -\rho D_{i,m} \nabla Y_i \quad (10)$$

In this equation $D_{i,m}$ is the diffusion coefficients for species i in the mixture. For diffusion dominated flows in the paper, the dilute approximation is not acceptable, full multi-component diffusion is required. In such case, The Maxwell-Stefan equations can be solved to obtain the binary diffusion coefficients.

5. Maxwell-Stefan equations

From Merk [29], the Maxwell-Stefan equations can be written as

$$\sum_{\substack{j=1 \\ j \neq i}}^N \frac{X_i X_j}{D_{ij}} \left(\frac{\vec{J}_j}{\rho_j} - \frac{\vec{J}_i}{\rho_i} \right) = \nabla X_i - \frac{\nabla T}{T} \sum_{\substack{j=1 \\ j \neq i}}^N \frac{X_i X_j}{D_{ij}} \left(\frac{D_{T,j}}{\rho_j} - \frac{D_{T,i}}{\rho_i} \right) \quad (11)$$

For an ideal gas the Maxwell diffusion coefficients are equal to the binary diffusion coefficients.

After some mathematical manipulations, the diffusive mass flux vector,

$$\vec{J}_i = -\sum_{j=1}^{N-1} \rho D_{ij} \nabla Y_j - D_{T,i} \frac{\nabla T}{T} \quad (12)$$

Where Y_j is the mass fraction of species j. Other terms are defined as follows:

$$D_{ij} = [D] = [A]^{-1} [B] \quad (13)$$

$$A_{ii} = -\left(\frac{X_i}{D_{iN}} \frac{M_w}{M_{w,N}} + \sum_{\substack{j=1 \\ j \neq i}}^N \frac{X_j}{D_{ij}} \frac{M_w}{M_{w,i}} \right) \quad (14)$$

$$A_{ij} = X_i \left(\frac{1}{D_{ij}} \frac{M_w}{M_{w,j}} - \frac{1}{D_{iN}} \frac{M_w}{M_{w,N}} \right) \quad (15)$$

$$B_{ii} = -\left(X_i \frac{M_w}{M_{w,N}} + (1 - X_i) \frac{M_w}{M_{w,i}}\right) \quad (16)$$

[A] and [B] are (N-1)×(N-1) matrices and [D] is an (N-1)×(N-1) matrix of the generalized Fick's law diffusion coefficients D_{ij} . M_w denotes the average molar mass of the mixture, and $M_{w,i}$, $M_{w,N}$ denotes the molar mass of species i and N .

With the use of the solution to the above governing equations, FLUENT can be set up to get the velocity and species concentration field for the opposed diffusion flow. The multi-component diffusion coefficients matrix was calculated based on the mass fraction in that grid. Gravity and buoyancy effects are taken into account in the momentum equation.

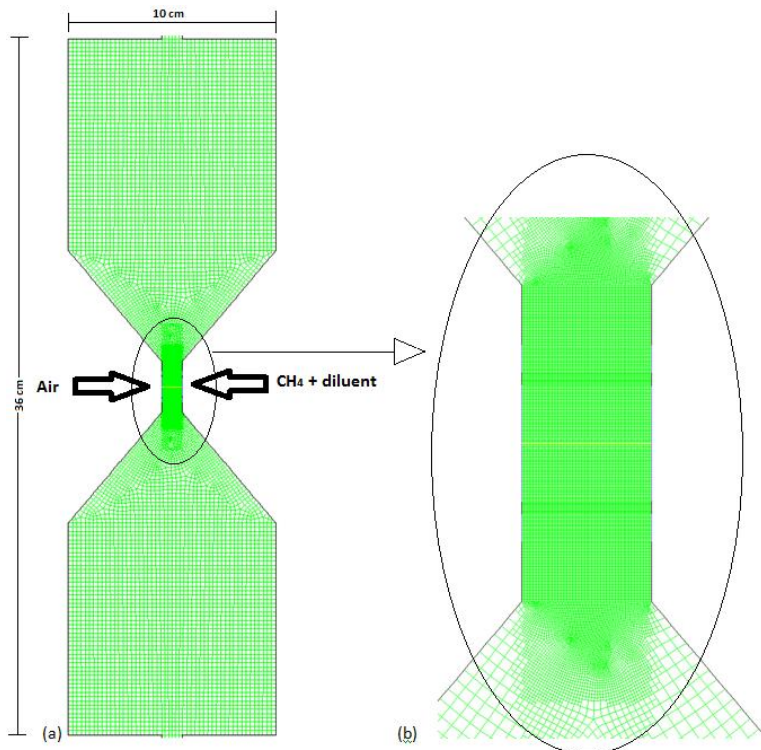


Figure 5 - (a) Calculation domain (b) Grid distribution

The calculation domain is shown in Figure 5, the domain size equals 10 cm in the axial direction by 36cm in the radial direction. The larger length is required to keep accuracy because a small length could affect the flow simulation results. The fuel and oxidizer burners are set with a diameter of 8.9mm, and the nitrogen flow is bounded by an inner diameter of 7.605 mm and an outer diameter of 13.56 mm. The oxidizer consists (in molar fraction) of 0.767 N₂ and 0.233 O₂ at room temperature 298.15K and 1 atm pressure. In Ref. [30] it is shown that the potential flow and plug flow has little effect on the velocity field in the mixing layer, so for simplicity, the fuel and oxidizer inlet are set to be velocity inlet with an average velocity.

Fuel and oxidizer flows were momentum-matched rather than velocity-matched. In momentum matched counterflow flames the position of the mixing layer region (i.e. ignitable region) lies around half the separation distance, thus very little movement is needed for optimal ignition conditions [15,23]. The high speed camera (Phantom v12.1) was set perpendicular to both the laser beam direction and the burner axis to capture the ignition process. These images allow determination of the time to flame kernel (or the ignition delay time) through the frame by frame playback as well as the time for the flame to become steady. This flame kernel is when chemical reactions have started and the temperature rises enough that it becomes visible. Once it is visible the ignition process has begun and a successful ignition is deemed when these reactions are sustained until the flame is steady. The data of the time to establish flame kernel (t_k) and to become steady for various global strain rates (K_g), diluents and dilution level were then obtained. The framing rate was 3,000 and the reported data are average of three to five runs. The repeatability lies with one or two frames, so the uncertainty of the temporal data is approximately 0.3-0.6 ms.

The imaging of the ignition events needed several iterations before the parameters described above

were chosen. The first step was to choose the best pixel configuration to visualize the section in between the burners where reactions take place with the TAMRON lens mentioned in section 3.1. In Table 2 the various possible configurations are given. In order to obtain the correct configuration physical adjustments of the camera's distance from the burner and height were necessary. The configuration that allowed for the best view was chosen to be 256 x 128 pixels. The next step was to choose a frame rate at which enough light was allowed into the sensor in order to be able to observe the ignition phenomena taking place. The framing rate was chosen to be 3,000 as mentioned above with the exposure time kept to the maximum allowed by the camera (332.89 μ s).

Imaging of the laser spark was performed to confirm the dimensions calculated. The image can be seen in Figure 6. The framing rate needed for this was determined to be 100,000. The spark was only visible for 1 frame. In order to get the correct distance to view the spark a small needle was placed at the location of the spark and the camera adjusted accordingly to observe it. The spark on the regular experiment setup (i.e. recording at 3000 fps) was identified as the frame in which the camera sensor was saturated. Due to the spark deposition time being so small, the experimental uncertainty temporal data ranges from 10-15%.



Figure 6 - Laser spark image using microscope lens

Table 2 – Phantom v12.1 pixels to maximum frames per second

Pixels	128	256	512	768	1024	1280
8	1,000,000	980,392	763,941	632,511	534,759	463,177
16	852,514	683,994	490,196	381,891	312,891	264,970
32	560,224	423,190	284,171	214,684	172,503	143,472
64	330,469	240,096	155,207	114,220	90,637	74,934
96	236,239	168,067	106,371	77,911	61,402	50,709
128	183,250	128,998	81,024	59,069	46,464	38,296
256	96,749	66,997	41,483	30,042	23,548	19,362
512	49,724	34,140	20,978	15,156	11,854	9,735
768	33,479	22,906	14,042	10,134	7,921	6,501
800	32,161	22,006	13,485	9,730	7,605	6,242

Limits of successful ignition (successful ignition is an event when a flame kernel develops into a steady flame) are defined as the strain rates above which no ignition is possible given the laser spark conditions. For the pure and diluted CH₄, such limits were obtained by gradually increasing the velocities of both reactant streams while simultaneously keeping the momentum-matched condition and the dilution level. Argon and Helium are chosen as diluents. They have the same volumetric heat capacity, but possess vastly different thermal and mass diffusivities. This difference permits to study of effects on ignition caused only by these transport properties rather than by the differences in their heat

capacities. The global strain rate, K_g , is defined, following Ref. [31], as

$$K_g = \frac{2V_o}{L} \left(1 + \frac{V_F}{V_o} \sqrt{\frac{\rho_F}{\rho_O}} \right) \quad (17)$$

where V_o , V_F , L , ρ_F , and ρ_O are, respectively, the velocities of oxidizer and fuel flows, the burner separation distance, the fuel-diluent mixture and air densities. The value of K_g beyond which the ignition failed is the limit of the global strain rate and is denoted by $K_{g,ig}$. In order to obtain extinction limit strain rates ($K_{g,ex}$, given in Table 3) the flame was ignited at low K_g and flow was gradually increased until extinction occurred. For comparison, the current value of $K_{g,ex} = 424 \text{ s}^{-1}$ (Table 3) for pure methane is in agreement with the published range of $400 \text{ s}^{-1} - 500 \text{ s}^{-1}$ [32].

Table 3 - Properties related to flame extinction and ignition of CH₄ and diluted CH₄

	Pure CH ₄	20%He	30%He	40%He	20% Ar	30%Ar	40%Ar
$D_t \text{ (m}^2\text{s}^{-1}\text{)}$	2.06×10^{-5}	2.31×10^{-5}	2.17×10^{-5}	2.70×10^{-5}	2.03×10^{-5}	2.04×10^{-5}	1.99×10^{-5}
$T_f^a \text{ (K)}$		1,755		1,690	1,780		1,750 [Ref. 20]
$T_{ad}^a \text{ (K)}$		2,214		2,187	2,211		2,185
$K_{g,ex} \text{ (s}^{-1}\text{)}$	575	405		250	575		480 [Ref. 20]
$K_{g,ex} \text{ (s}^{-1}\text{)}$	424	312		161	376		352
$K_{g,ig} \text{ (s}^{-1}\text{)}$	380	272	178	110	349	330	328
$S_L \text{ (ms}^{-1}\text{)}$	0.355	0.362	0.365	0.374	0.352	0.347	0.345
$\delta^b \text{ (m)}$	1.89×10^{-4}	2.10×10^{-4}	2.50×10^{-4}	3.30×10^{-4}	1.85×10^{-4}	2.11×10^{-4}	2.12×10^{-4}
Da_{ig}	3.26	3.29	4.21	4.56	3.21	3.58	3.68

^a T_{ad} is the adiabatic flame temperature and T_f is the counter-flow flame temperature near-extinction

^b calculated at $K_g = K_{g,ig}$

CHAPTER 4: ANALYSIS

4.1 Ignition position

In Fig. 7 the ignition positions calculated by FLUENT V6.3 software are shown. The governing equations used for these calculations are given in Chapter 3 of this thesis. It can be observed that ignition position is not only a function of diluents type and dilution level (both affect the value of Y_{st}), but that it is a function of strain rate as well. Since $Y_{st} < 0.055$ (0.055 is the value of Y_{st} for pure CH_4), then the ignition location lies on the air side of the mixing layer. It can also be observed that as dilution level is increases (i.e., Y_{st} is decreased), the ignition position moves closer to the mid-plane between the nozzles on the counter-flow burner. For a given dilution level, the ignition location for Ar-diluted fuel is closer to the mid-plane than the He-diluted fuel, as the former produces smaller values of Y_{st} .

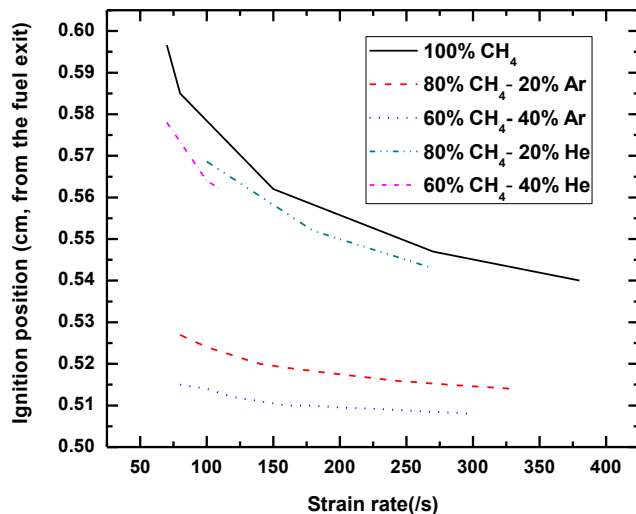


Figure 7 - Ignition position vs. global strain rate

4.2 Visual observations

In the experiment shown in Fig. 8 pure methane was used on the fuel side. The flows were not momentum-matched using the description given in Chapter 3 because at the time the goal was to obtain a successful ignition event. In this case a velocity was chosen for air and the equivalent counterpart for fuel was estimated using the respective conversion parameters of the flow meters for methane, thus the flame ended up lying closer to the fuel side. Experiments performed afterward using the methodology given in Chapter 3 resulted in flames lying on the air side. The strain rate of this experiment was calculated to be 300 s^{-1} . The location of the spark to achieve the ignition was at the mid-plane (0.5 cm from bottom burner), but no time data was recorded on this first trial. Lastly, it also provided the first insight (effects of ignition location on repeatability, calibration of flow meters to assure proper readings) into what was necessary to conduct a successful experiment (i.e. establish an experimental procedure and the importance of optimal ignition location).



Figure 8 - First successful ignition of counter-flow flame in this work

Typical images for the CH₄ fuel and fuel-inert mixtures from the high-speed photography of the ignition process are reported in Fig. 9, where the laser spark was initiated at $t = 0$ and t_k denotes the time when the first sign of flame kernel appeared. Images denoted by (d) are believed to be of the flames that had achieved the steady state. Using Fig. 9 as the example, ignition processes showing images (a) that eventually lead to images (d) (i.e. go from the flame kernel to steady flame) are termed as successful ignition.

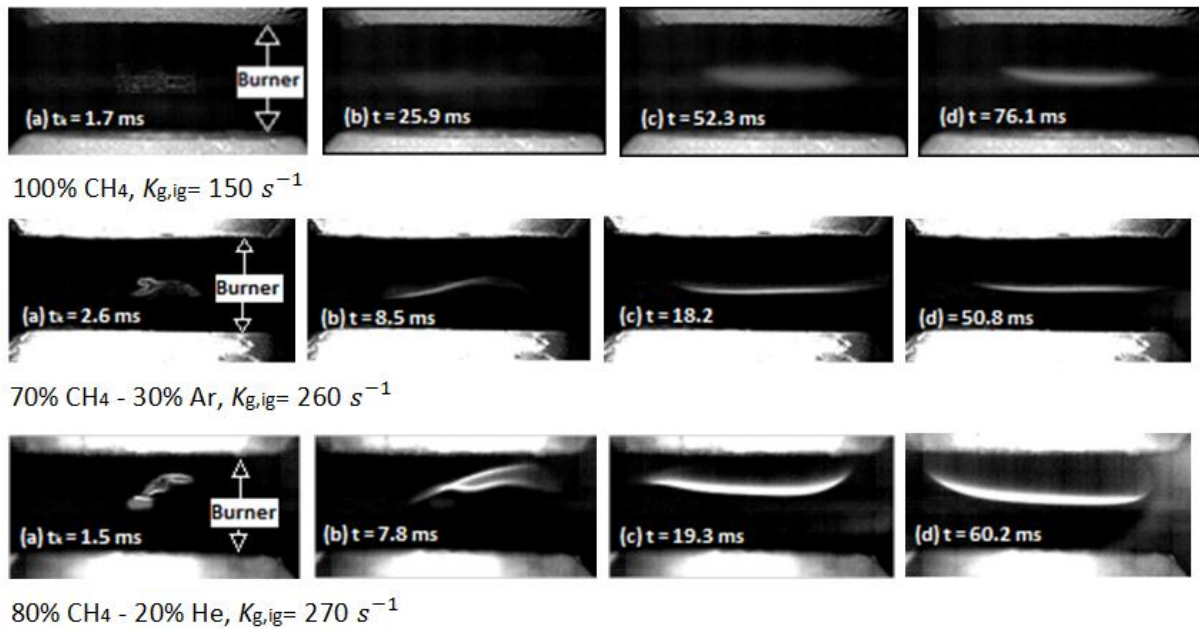


Figure 9 - Ignition process ($t = 0$ at spark deposition) – (a) Identification of time to flame kernel formation (Processed with ImageJ to enhance visibility); (b) & (c) flame development process; (d) time to steady flame.

4.3 Critical strain rate, $K_{g,ig}$

The time to flame kernel data (t_k) for all the fuel-inert mixture studied (listed in Table 3) are presented as a function of K_g in Fig. 10 in order to understand how changes in flow conditions as well as changes in thermal diffusive properties (i.e. dilution level) affect ignition phenomena. Because Fig. 10 reports t_k for all successful ignition for the given laser spark energy, the end points (maximum K_g) for each fuel-inert mixture also represent values of $K_{g,ig}$. The effect of effective Lewis number (Le_e) on $K_{g,ig}$ is here discussed first (Eq. 1), as it is known to successfully explain the global extinction strain rates ($K_{g,ex}$) for methane fuels diluted with helium and argon at various dilution levels [20]. This effective Lewis number (Le_e) (Eq. 1) takes into account the combined (non-stoichiometric) mixture of fuel, oxidizer and diluents as the ratio of the mixture thermal diffusivity to the mass diffusivities of fuel and oxidizer for mixtures studied (Table 4) (which are evaluated at room temperature and pressure). Le_f (Table 4) is the more traditional definition of Lewis number used, but it does not take into account the oxidizer, which is the reason why Le_e is used.

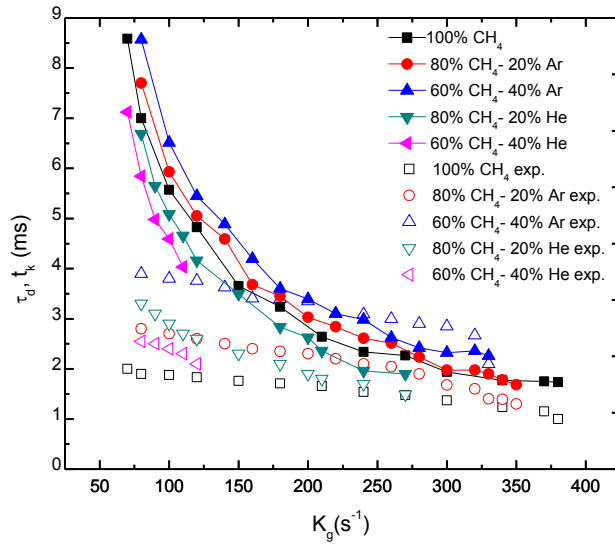


Figure 10 - Time to flame kernel (t_k ; open symbols) and characteristic thermal diffusion time (τ_d ; closed symbols) vs. global strain rate

Table 4 - Effective and fuel Lewis number for various dilution levels

	20%	30%	40%	50%
Le_f -He	0.489	0.586	0.700	0.857
Le_e -He	1.246	1.319	1.397	1.478
Le_f -Ar	1.085	1.058	1.041	1.021
Le_e -Ar	1.075	1.060	1.049	1.039

The results in Table 3 also show that for the dilution levels studied, diluted fuels possess smaller values of $K_{g,ex}$ than the pure fuel. As a result from using different diluents and dilution levels, the effect of Le_e on extinction $K_{g,ex}$ can be summarized as follows. With the same level of dilution, the diluents

producing smaller values of Le_e yield larger values of $K_{g,ex}$. Dilution with Ar produces smaller values of Le_e and larger values of $K_{g,ex}$ than with He for both 20% and 40% dilution. For example, 40% dilution with He/Ar leads to $Le_e = 1.397/1.049$ and $K_{g,ex}=161 \text{ s}^{-1}/352 \text{ s}^{-1}$.

These results are consistent with those from Ref. [20] using different counter-flow burners, which are reproduced and given in Table 4. They suggest that $K_{g,ex}$ is affected not only by dilution that simply lowers the flame temperature and reaction rate, but also on the relative rate of diffusion of chemical and thermal enthalpy in the into and out of the reaction zone, i.e., on Le_e . As shown in Tables 3 and 4, with the same level of dilution, the diluent producing smaller values of Le_e also yields larger values of T_f , the flame temperature. For example in Table 3 for 40% dilution level T_f for the Ar diluted flame is 1750 K ($Le_e = 1.049$) and for the He diluted flame T_f is 1690 K ($Le_e = 1.397$). In the following paragraph the effect of Le_e on $K_{g,ig}$ is discussed given the laser spark energy.

The experimental value of $K_{g,ig}$ for the fuel-inert mixtures shown in Table 3 has a maximum value for pure CH_4 , as expected. Ar-diluted mixtures have larger value of $K_{g,ig}$ compared to the He-diluted mixtures and the difference appears to be larger as the difference in Le_e is larger – the 40% dilution results in a larger difference in Le_e (1.049 for Ar diluted flame and 1.397 for He diluted flame) and larger difference in $K_{g,ig}$ (328 s^{-1} for 40% Ar and 110 s^{-1} for 40% He) with the Ar-diluted mixture having a smaller Le_e and larger $K_{g,ig}$. It is also noted that for a given diluent and dilution level, $K_{g,ig} < K_{g,ex}$. $K_{g,ig}$ is expected to be smaller than $K_{g,ex}$ if the Damköhler number is defined as the ratio of characteristic flow time ($\tau \propto 1/K_g$) to characteristic chemical reaction time, then $Da_{ex} \equiv 1/(K_g \tau_c)$. For a given diluent and level of dilution τ_c is known. Therefore, $Da \propto 1/K_g$. Thus, the ignition Damköhler number is larger than the extinction Damköhler number, consistent with Liñan's S-curve for diffusion flames [33].

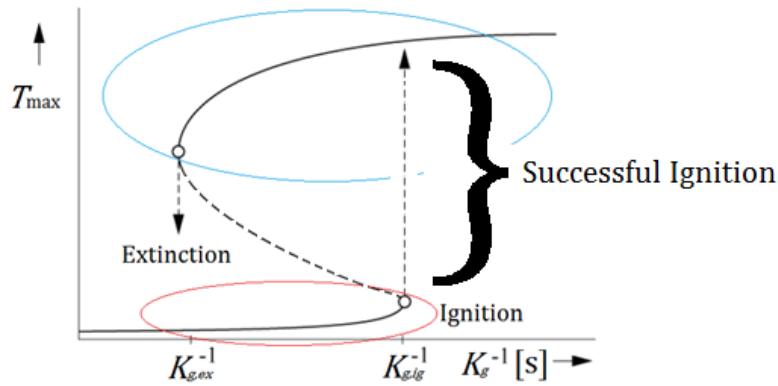


Figure 11 - S-curve for diffusion flames

In Fig. 11 the behavior of temperature related to the inverse of strain rate is shown. This figure is based on Liñan's work [33], who investigated the structure of steady state diffusion flames by analyzing the mixing and chemical reaction of two opposed jets of fuel and oxidizer. The maximum temperature is given in terms of Damköhler number (as stated before $Da \propto 1/K_g$) and resulted in the S-curve shown above. The upper part of the S-curve in Fig. 11 (circled in blue) represents the change in Damköhler as strain rate is increased (i.e. move along the curve towards the left) with the flame already existing. Meanwhile on the bottom part of Fig.11 (circled in red) it starts at room condition (i.e. low T, P) and as ignition occurs (from flame kernel to steady flame) there is a temperature jump to the steady flame regime. After successful ignition the upper right part of the curve represents the flame.

Two limits are observed in Fig. 11, one for ignition and the other for extinction. Once ignited temperature in the flammable layer rapidly increases until flame is steady, but once $K_{g,ig}$ is reached ignition is not possible anymore. In extinction a flame already exists and K_g is slowly increased until $K_{g,ex}$ is reached. At $K_{g,ex}$ temperature rapidly drops and the flame no longer exists. The behavior in

Liñan's S-curve coincides with the finding in this work that $K_{g,ig} < K_{g,ex}$. This is due to the asymptotic structure of diffusion flames, and both limits found in different parts of the curve. It is of interest in this work to concentrate on the lower part of the S-curve and find what factors are present for the critical Damköhler number for ignition, which is discussed next.

4.4 Critical Damköhler number for ignition

Fig. 10 shows variation of τ_d as a function of diluents and dilution level from calculations using FLUENT (in solid symbols). τ_d can be regarded as the time limit within which the successful ignition is possible before energy is dissipated out of the flammable layer and its definition can be seen in Eq. 18:

$$\tau_d = \frac{\delta^2}{D_t} \quad (18)$$

δ and D_t are the flammable layer thickness and thermal diffusivity, respectively. In Fig. 10 it is noticed that under lower strain rate (60-100/s), values of τ_d are far larger than the experimental results for time to flame kernel (t_k), while the differences decrease at higher strain rate (>100/s). The reason being that at low strain rates, the convection is not strong and the thickness of the flammable layer is larger (Fig. 12), consequently a larger time window to obtain a flame kernel is ensured. As strain rate is increased, the convection of the counter flows become stronger and values of δ of the methane diluted flames decrease, thus reducing τ_d .

While flow time scale (inversely proportional to global strain rate) may be used to define Damköhler number, for successful ignition of the flammable mixture in the mixing layer the heat generation rate must exceed the heat loss rate. This means that the thermal diffusion time scale (τ_d) and the chemical reaction or induction time scale (τ_c) following energy deposition by the laser spark should be on the

same order of magnitude at ignition. The characteristic values of τ_c and τ_d are proportional, respectively, to δ/S_L and δ^2/D_t where δ , S_L , and D_t are, respectively, the flammable layer thickness, the one-dimensional laminar flame propagation speed for stoichiometric fuel-air mixtures, and thermal diffusivity of the fuel-air-inert mixture in the mixing layer. Therefore, the critical Damköhler number for ignition can be defined as

$$Da_{ig} \equiv \frac{\tau_d}{\tau_c} \approx \frac{\delta}{D_t S_L} \quad (19)$$

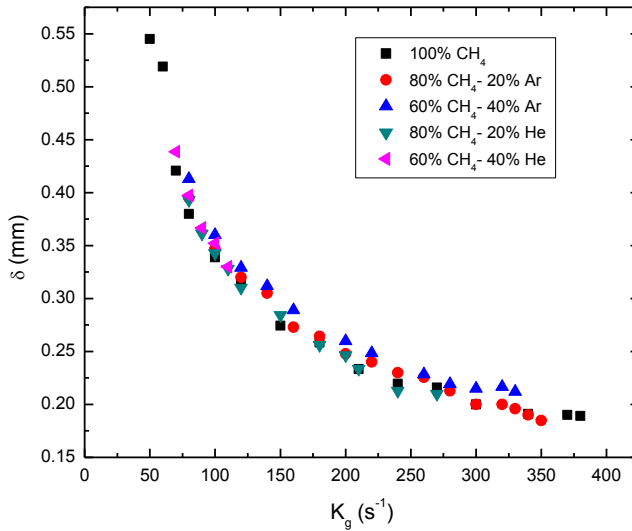


Figure 12 - Flammable layer thickness vs. global strain rate

In the counter-flow configuration, the value of δ is that of the region bounded by lean and rich flammability limits of methane-air mixtures (equal to, respectively, 5% and 15% fuel volume fraction [34], which translate to equivalence ratio $\phi_{lean}=0.5164$ and $\phi_{rich}=1.6182$). Due to dilution, the value of δ varies with diluent type, dilution level, and K_g . The values of δ were calculated for cold flows using the FLUENT software with their results shown in Fig. 11, as functions of diluent type, dilution level, and

K_g . Values of S_L were found using CHEMKIN with GRI-Mech 3.0 and are listed in Table 3 along with values of δ corresponding to $K_{g,ig}$. D_t values were calculated using FLUENT and are also listed in Table 3.

Values of Da_{ig} for the fuel and fuel-inert mixtures shown in Table 3 appear to be on the same order of magnitude and ranges from approximately 3.2 to 4.6. The 40% He-diluted mixture has a larger value of Da_{ig} (by approximately 30%) than the other mixtures, as it has the smallest $K_{g,ig}$ (110 s^{-1} , Table 3). With Ar, having similar diffusivities as the pure CH_4 (in the range of $2 \times 10^{-5} \text{ m}^2\text{s}^{-1}$, Table 3), the value of δ is expected to be insensitive to dilution. For diluent having large diffusivities, such as helium, the physical boundaries of ϕ_{lean} and ϕ_{rich} may enlarge, as the result in Table 3 show that with 40% helium, $\delta = 3.30 \times 10^{-4} \text{ m}$, approximately 50% larger than other fuels, resulting an approximately 30% larger value of Da_{ig} than other fuel mixtures, consistent with Eq. (6), where values of S_L and D_t do not vary much among all fuel mixtures (see Table 3).

The alternative definition of Damköhler number for ignition is to use the characteristic flow time ($\tau \propto 1/K_g$), as customarily done for extinction studies ($Da = 1/(K_g\tau_c)$). In Fig. 13 τ_d and $1/K_g$ can be seen to correlate in a linear manner, i.e., $1/K_g \approx c\tau_d$, with the constant c falling in the range of approximately 1.5 – 2. Thus when the alternative definition is used we know τ_c for given diluents and dilution level and the value of Da_{ig} falls in the range of approximately 5 – 9. As can be seen in Fig. 13 for 40% helium dilution, the value of c is the largest further amplifying the difference in Da_{ig} among the fuel mixtures. However, with either definition the values of Da_{ig} for the fuels mixtures studied are of the same order of magnitude.

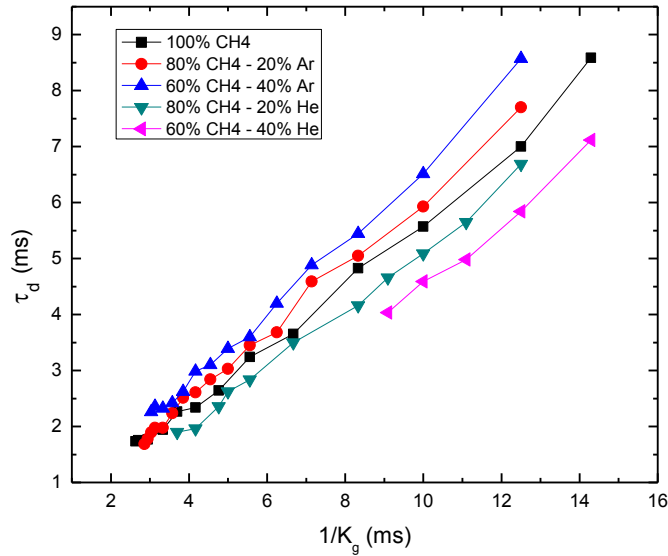


Figure 13 - Thermal diffusion time scale vs. convective flow time scale

In summary, for the same level of dilution the diluent generating a smaller Le_e (argon) results in larger $K_{g,ig}$ and $K_{g,ex}$. In other words, the diluent giving a smaller Le_e causes the flame more resistant to extinction and makes successful ignition easier to achieve (i.e., achievable at higher strain rates). However, when the thermal diffusion and chemical time scales are considered, the vastly apparently different values in $K_{g,ig}$ leads to similar values of Da_{ig} -- the maximum difference in Da_{ig} are with 40% helium and argon whose values of $K_{g,ig}$ are 110 s^{-1} and 328 s^{-1} , a three-fold difference, while their values of Da_{ig} have a merely 20% difference (4.56 vs. 3.68).

4.5 Time to flame kernel/induction time, t_k

While Ar-diluted flames are more resistant to extinction by strain and its mixtures can be ignited at larger $K_{g,ig}$, they nonetheless have larger values of t_k than the He-diluted mixtures at the same level of

dilution. This observation holds for all range of K_g reported in Fig. 10. The molecular relaxation time was initially suspected to cause differences in values of t_k , because Ar has the largest rotational/translation time among the possible molecules (CH_4 , He, H_2O , CO_2 , O_2 , and N_2) present in the mixing layer (10^{-5} s [35-39]). However, the typical values of t_k reported are several milliseconds and, therefore, should not be affected by molecular relaxation due to the laser pulse. Therefore, the values of t_k reported in Fig. 10 are dependent on dilution and transport properties resulting from dilution.

The value of t_k for pure CH_4 is the lowest among all fuels throughout the entire range of K_g , as expected. For the same dilution level (i.e., the effect of thermal capacity are the same for helium and argon), Ar-diluted mixture leads to larger values of t_k , suggesting that smaller values of Le_e lead to larger t_k . As shown in Fig. 10, increasing the argon dilution level from 20% to 40% increases t_k by a factor of approximately 2 over the reported range of K_g , while increasing the helium dilution level from 20% to 40% leads to a decrease in t_k . Thus, the effect of increasing the dilution level with He leads to somewhat unexpected results of t_k .

These trends appear to be not explainable by the effect of Lewis number, either. This is because as dilution for He is increased from 20% to 40%, Le_e increases from 1,246 to 1.396 and the diffusive-thermal effect should lead to decrease in mixture temperature not only because of dilution effect but also because of larger rates of thermal diffusion away from the mixture (i.e., cooling) than the heat generation rate from chemical reaction. It is desirable to examine the role of τ_d – one expects that if $t_k > \tau_d$, then there would be no successful ignition and no value of t_k should be or can be reported. Thus, it is reasonable to expect $t_k < \tau_d$. Since the *characteristic* (rather than the absolute) time scale is of interest, the ratio t_k/τ_d was calculated using the data in Fig. 10 (ratio of open to closed symbols) as well as data obtained for dilution levels of 30 and 50 percent for both diluents. The results are shown in Fig. 14.

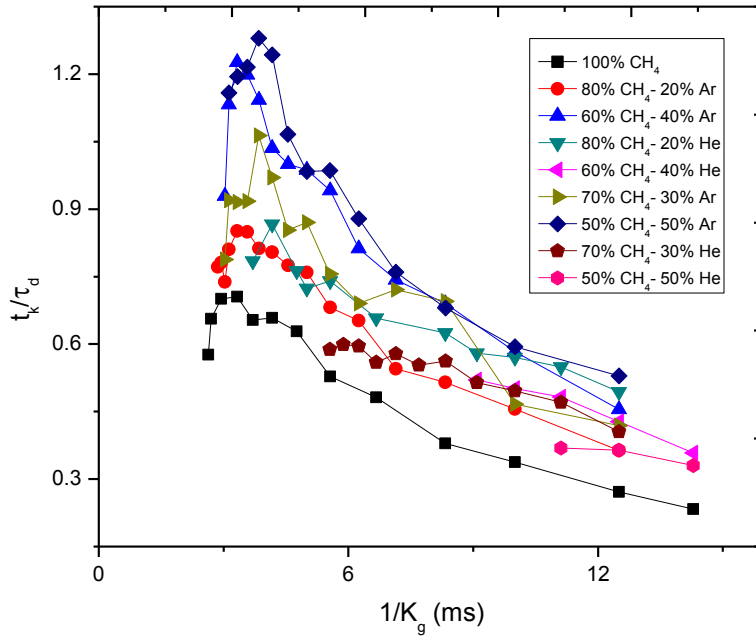


Figure 14 - Non-dimensional ignition to diffusion time vs. global flow time

The results of Fig. 14 suggest that as the flow time $1/K_g$ is reduced, the ratio t_k/τ_d increases. As a consequence, as τ_d is decreased, t_k increases relative to the time ignition has to be successful, despite the fact that t_k decreases with increasing K_g , as Fig. 10 indicates. Thus, although increasing K_g leads to smaller t_k , ignition eventually fails because the decrease in τ_d with increasing K_g outpaces the decrease in t_k .

The reason for infeasible Lewis number explanation for the He-diluted mixture might be given as follows. Due to the much larger thermal diffusivity of He, as the dilution level is increased, τ_d decreases resulting in a higher heat transfer and cooling rate from the flammable layer (as can be seen from Fig. 11). This causes a decrease in chemical reaction rate. As a consequence, t_k increases from 20% to 40%

dilution for K_g up to $K_{g,ig}$ (see Fig. 10). Furthermore, the value of $K_{g,ig}$ is much smaller with 40% He dilution, further suggesting the thermal cooling due to He. For successful ignition, these results suggest that (1) simple effect of dilution (such as by argon) leads to an increase in t_k and (2) decreasing τ_d (such as by increasing dilution level with helium) forces smaller t_k if ignition occurs but results in smaller $K_{g,ig}$ (i.e., more difficult to ignite under moderate strain rates).

4.6 Time to steady flame

The other transient event recorded in this study is the time for the flame to become steady. This time is defined as the time necessary for the flame not to exhibit any visible major changes in structure, brightness or other characteristics. Once the flame had been observed for 10 – 15 frames without such changes being observed, the flame was deemed steady. In Fig. 15 time to steady flame for all cases in this work is observed as function of global strain rate. In all cases the time to steady flame has been observed to decrease as strain rate is increased. The flame quickly expands in the flammable layer as the characteristic diffusion time is reduced (i.e. K_g increases) and any events taking place outside of this region are quickly diffused.

In Fig. 15 it can be observed that for He diluted flames the times to steady flame increased more significantly with the increase of dilution level than those of their Ar diluted counterparts. This is to be expected due to the larger thermal diffusivity of He, thus thermal diffusion for He is larger than for Ar. Also can be noted that for cases where experiments with strain rates higher than 200 s^{-1} were possible, the times to steady flame seem to converge closely together and even some crossing can be observed. Several attempts to explain why this is the case have been made, including calculations of Richardson number (Fig. 16) to see whether buoyancy affected the flow, but the results were inconclusive.

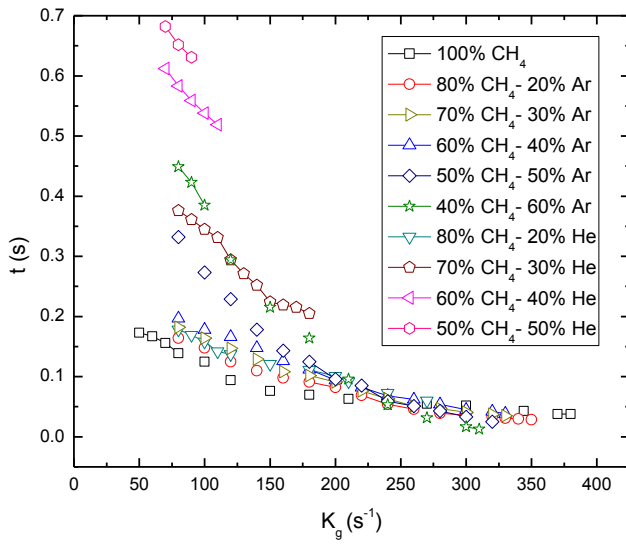


Figure 15 - Time to steady flame vs. global strain rate

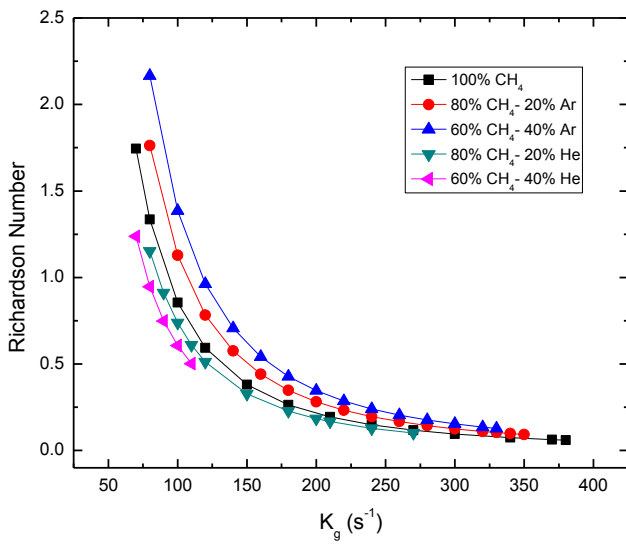


Figure 16 - Richardson number vs. global strain rate

CHAPTER 5: CONCLUSION

5.1 Summary

In this thesis the effects of transport properties, effective Lewis number and thermal diffusivities, on ignition, ignition time (t_k) and time to steady flame of counter-flow diffusion flames have been investigated. The variations in transport properties were obtained by using helium and argon as diluents. Several conclusions and contributions can be made from this work and are presented in the following paragraphs.

The role of effective Lewis number (Le_e) on the maximum global strain rate ($K_{g,ig}$), beyond which ignition is not possible, is found to be qualitatively similar to that on the extinction strain rate. With the same level of dilution, the inert diluent with smaller Le_e yields larger $K_{g,ig}$. With the fuel-inert mixtures, the critical ignition Damköhler numbers fall within 20%-30% of each other. While Le_e is a viable parameter to explain $K_{g,ig}$ results, no consistent role of Le_e on t_k has not been found.

Argon has similar thermal diffusivity (D_t) as other species in the flammable layer and, thus increasing its dilution level (from 20% to 40% argon) leads to larger t_k due to the lowering of the temperature during the ignition process. For He, the opposite is true due to its much larger thermal diffusivity that leads to cooling during the ignition process. In summary, the cooling effect results from both dilution and thermal diffusion – for argon, increasing dilution level leads to lower temperatures and for helium increasing dilution level leads to smaller τ_d , under which successful ignition needs to occur in shorter time (thus, smaller t_k) and can occur only with smaller strain rates.

Lastly, time to steady flame experiment data resulted in some expected behavior (decreases as strain rate increases) due to the thickness reduction of the flammable layer. Also observed was the more pronounced effects of thermal cooling on He diluted flames compared to their Ar counterparts. Also observed was the convergence of time to steady flame in experiments where ignition on strain rates above 200 s^{-1} was possible. For this case, no parameters that govern their behavior have been found.

5.2 Future work

The work presented in this thesis is the first step into gaining a deeper understanding of phenomena that occurs during ignition of turbulent diffusion flames as well as the effects of diluents and diffusive-thermal properties in ignition phenomena in these flames. The experimental results presented here for both time to flame kernel as well as time to steady flame will serve as validation as computational transient models are developed to reciprocate the events described in this work. Once an effective model involving detailed chemical kinetics is created more insight could be gained into all flow, chemical and other events that take place during the ignition process. Due to the large amount of calculations needed to simulate these events with detailed kinetics large computational power will be required.

PUBLICATION LIST

- Fidelio Sime Segura, Yan Wei, Ruey-Hung Chen, and Weiwei Deng. "LASER SPARK IGNITION OF COUNTER-FLOW DIFFUSION FLAMES: EFFECTS OF DILUENTS AND DIFFUSIVE-THERMAL PROPERTIES." *International Symposium on Combustion 34th* (2012). Under review.
- Fidelio Sime Segura, Yan Wei, Ruey-Hung Chen, and Weiwei Deng. "Laser Spark Ignition of Counterflow Diffusion Flames with Diluents." *US National Combustion Meeting 7th* (2011). Poster.

REFERENCES

- [1] Williams, Forman A. *Combustion Theory: The Fundamental Theory of Chemically Reacting Flow Systems*. Menlo Park, CA [etc.: Benjamin/Cummings, 1985.
- [2] Bradley, John N. *Flame and Combustion Phenomena*. London: Methuen, 1969.
- [3] Johnson, R. G., A. C. McIntosh, and J. Brindley. "Extinction of Premixed Flames by Pressure Drops." *Combustion and Flame* 102.4 (1995): 493-500.
- [4] Sohrab, S., and C. Law. "Extinction of Premixed Flames by Stretch and Radiative Loss." *International Journal of Heat and Mass Transfer* 27.2 (1984): 291-300.
- [5] "USCEI: The USC Energy Institute." *USC Energy Institute*. Web. 05 Mar. 2012.
- [6] Williams, F. A. "Turbulent Mixing in Non-Reactive and Reactive Flows." *Plenum* (1975): 189.
- [7] Mastorakos, E. "Ignition of Turbulent Non-premixed Flames." *Progress in Energy and Combustion Science* 35 (2009): 57-97.
- [8] Phuoc, T. X. "Laser Spark Ignition: Experimental Determination of Laser-induced Breakdown Thresholds of Combustion Gases." *Optics Communications* 175 (2000): 419-23.
- [9] Phuoc, T., and R. Chen. "Use of Laser-induced Spark for Studying Ignition Stability and Unburned Hydrogen Escaping from Laminar Diluted Hydrogen Diffusion Jet Flames." *Optics and Lasers in Engineering* 45.8 (2007): 834-42.
- [10] Richardson, E. S., and E. Mastorakos. "Numerical Investigation Of Forced Ignition In Laminar Counterflow Non-Premixed Methane-Air Flames." *Combustion Science and Technology* 179.1-2 (2007): 21-37.

- [11] Phuoc, T. X. "Laser-induced Spark Ignition Fundamental and Applications." *Optics and Lasers in Engineering* 44.5 (2006): 351-97
- [12] Phuoc, T. X., C. M. White, and D. H. McNeill. "Laser Spark Ignition of a Jet Diffusion Flame." *Optics and Lasers in Engineering* 38 (2002): 217-32. X. Phuoc. Laser-induced spark ignition fundamental and applications. *Optics and Lasers in Engineering* 2006; 44:351-397
- [13] Seshadri, K., C. Trevino, and M.d. Smooke. "Analysis of the Structure and Mechanisms of Extinction of a Counterflow Methanol-air Diffusion Flame." *Combustion and Flame* 76.2 (1989): 111-32.
- [14] Tsuji, H., A. Yoshida, and N. Endo. "Effect of Turbulence on Extinction of Counterflow Diffusion Flame." *Symposium (International) on Combustion* 25.1 (1994): 1191-197.
- [15] Dixon-Lewis, G., and M. Missaghi. "Structure and Extinction Limits of Counterflow Diffusion Flames of Hydrogen-nitrogen Mixtures in Air." *Symposium (International) on Combustion* 22.1 (1989): 1461-470.
- [16] Kitajima, A., T. Ueda, A. Matsuo, and M. Miomoto. "Experimental Investigation of the Flame Structure and Extinction of Turbulent Counterflow Non-premixed Flames." *Symposium (International) on Combustion* 26.1 (1996): 137-43.
- [17] Liu, F., G.j. Smallwood, Ö.I. Gülder, and Y. Ju. "Asymptotic Analysis of Radiative Extinction in Counterflow Diffusion Flames of Nonunity Lewis Numbers." *Combustion and Flame* 121.1-2 (2000): 275-87.
- [18] Wang, H. Y., W. H. Chen, and C. K. Law. "Extinction of Counterflow Diffusion Flames with Radiative Heat Loss and Nonunity Lewis Numbers." *Combustion and Flame* 148.3 (2007): 100-16.
- [19] Fotache, C. G., T. G. Kreutz, and C. K. Law. "Ignition of Hydrogen-enriched Methane by Heated Air." *Combustion and Flame* 110.4 (1997): 429-40.

- [20] Chen, Ruey-Hung, Marcos Chaos, and Anupam Kothawala. "Lewis Number Effects in Laminar Diffusion Flames near and Away from Extinction." *Proceedings of the Combustion Institute* 31.1 (2007): 1231-237.
- [21] Park, J., D. H. Lee, S. H. Yoon, and Et Al. "Effects of Lewis Number and Preferential Diffusion on Flame Characteristics in 80% H₂/20%CO Syngas Counterflow Diffusion Falmes Diluted with He and Ar." *International Journal of Hydrogen Energy* 34 (2009): 1578-584.
- [22] Li, Zhiliang, Ruey-Hung Chen, and Tran X. Phuoc. "Effects of Multi-component Diffusion and Heat Release on Laminar Diffusion Flame Liftoff." *Combustion and Flame* 157.8 (2010): 1484-495.
- [23] Kim, J. S., and S. R. Lee. "Diffusional-thermal Instability in Strained Diffusion Flames with Unequal Lewis Numbers." *Combustion Theory and Modelling* 3.1 (1999): 123-46.
- [24] Coppola, Gianfilippo, Bruno Coriton, and Alessandro Gomez. "Highly Turbulent Counterflow Flames: A Laboratory Scale Benchmark for Practical Systems." *Combustion and Flame* 156 (2009): 1834-843.
- [25] Eckstein, J. "Modeling of Turbulent Mixing in Opposed Jet Configuration: One-dimensional Monte Carlo Probability Density Function Simulation." *Symposium (International) on Combustion* 28.1 (2000): 141-48.
- [26] Bindhu, C.V., S.S. Harilal, M.S. Tillack, F. Najmabadi, and A.C. Gaeris. "Energy Absorption and Propagation in Laser-Created Sparks." *Applied Spectroscopy* 58.6 (2004): 719-26.
- [27] Phuoc, Tran X., and Fredrick P. White. "Laser-induced Spark Ignition of CH₄/air Mixtures." *Combustion and Flame* 119.3 (1999): 203-16.
- [28] Batchelor, G. K. *An Introduction to Fluid Dynamics*,. Cambridge: U.P., 1967.
- [29] Merk, H. J. "The Macroscopic Equations for Simultaneous Heat and Mass Transfer in Isotropic, Continuous and Closed Systems." *Applied Scientific Research* 8.1 (1959): 73-99.

- [30] Sung, C. J., J. B. Liu, and C. K. Law. "Structural Response of Counterflow Diffusion Flames to Strain Rate Variations." *Combustion and Flame* 102.4 (1995): 481-92.
- [31] Seshadri, K., and F. A. Williams. *International Journal of Heat and Mass Transfer* 21 (1978): 251-53.
- [32] Lazzarini, A. K., R. H. Krauss, and H. K. Chelliah. "Extinction of Counterflow Diffusion Flames with Fine-water Droplets." *Proceedings of the Combustion Institute* (2000): 2939-945.
- [33] Liñán, A. "The Asymptotic Structure of Counterflow Diffusion Flames for Large Activation Energies." *Acta Astronautica* 1.7-8 (1974): 1007-039.
- [34] Glassman, Irvin, and Richard A. Yetter. *Combustion*. Amsterdam: Elsevier, 2008.
- [35] Kistemaker, P. G. "Rotational Relaxation in Mixtures of Methane with Helium, Argon and Xenon." *Physica* 60 (1972): 459-71.
- [36] Trunec, D., P. Spanel, and D. Smith. "The Influence of Electron–electron Collisions on Electron Thermalization in He and Ar Afterglow Plasmas." *Chemical Physics Letters* 372.5-6 (2003): 728-32.
- [37] Carroll, T. O., and S. Marcus. "A Direct Measurement of the Rotational Relaxation Time in CO₂." *Physics Letters A* 27.9 (1968): 590-91.
- [38] Kistemaker, P. G., and A. E. De Vries. "Rotational Relaxation times in Nitrogen-noble-gas Mixtures." *Chemical Physics* 7.3 (1975): 371-82.
- [39] Blackman, Vernon. "Relaxation in Oxygen and Nitrogen." *Journal of Fluid Mechanics* 1.01 (1956): 61.